



**HAL**  
open science

## Palaeomagnetism of the upper volcanic supergroup, southern part of the Sierra Madre Occidental, Mexico

Mireille M. Perrin, L. M. Alva-Valdivia, M. Lopez-Martinez, J. Rosas-Elguera,  
M. Benammi, J. A. Gonzalez-Rangel, Pierre Camps

► **To cite this version:**

Mireille M. Perrin, L. M. Alva-Valdivia, M. Lopez-Martinez, J. Rosas-Elguera, M. Benammi, et al.. Palaeomagnetism of the upper volcanic supergroup, southern part of the Sierra Madre Occidental, Mexico. *Geophysical Journal International*, 2013, 193 (3), pp.1250-1264. 10.1093/gji/ggt079 . hal-00854457

**HAL Id: hal-00854457**

**<https://hal.science/hal-00854457>**

Submitted on 19 Oct 2020

**HAL** is a multi-disciplinary open access archive for the deposit and dissemination of scientific research documents, whether they are published or not. The documents may come from teaching and research institutions in France or abroad, or from public or private research centers.

L'archive ouverte pluridisciplinaire **HAL**, est destinée au dépôt et à la diffusion de documents scientifiques de niveau recherche, publiés ou non, émanant des établissements d'enseignement et de recherche français ou étrangers, des laboratoires publics ou privés.

## Palaeomagnetism of the upper volcanic supergroup, southern part of the Sierra Madre Occidental, Mexico

M. Perrin,<sup>1</sup> L.M. Alva-Valdivia,<sup>2</sup> M. Lopez-Martinez,<sup>3</sup> J. Rosas-Elguera,<sup>4</sup> M. Benammi,<sup>5</sup> J.A. Gonzalez-Rangel<sup>2</sup> and P. Camps<sup>6</sup>

<sup>1</sup>*CEREGE, CNRS and Aix-Marseille Université UM34, 13545 Aix en Provence, France. E-mail: perrin@cerege.fr*

<sup>2</sup>*Laboratorio de Paleomagnetismo, Instituto de Geofísica, Universidad Nacional Autónoma de México, Ciudad Universitaria, 04510 Mexico DF, Mexico*

<sup>3</sup>*Department of Geología, CICESE, Carr. Ensenada-Tijuana No 3918, Ensenada, B.C., CP 22860, Mexico*

<sup>4</sup>*División de Ingenierías, Centro Universitario de Ciencias Exactas e Ingenierías, Universidad de Guadalajara, Av. Revolución No. 1500, Guadalajara, Mexico*

<sup>5</sup>*IPHEP, CNRS, 40 av. Recteur Pineau, 86022 Poitiers Cedex, France*

<sup>6</sup>*Géosciences Montpellier, CNRS and Université Montpellier 2, 34095 Montpellier, France*

Accepted 2013 February 25. Received 2013 February 23; in original form 2012 August 28

### SUMMARY

Ash flow tuffs, or ignimbrites have been recently proposed to be a good material for palaeointensity determination. In this paper, we present a multidisciplinary study, combining geochronology, petrology, rock magnetism and palaeomagnetism, carried out on Oligocene to Early Miocene ignimbrites and related flows from the southern part of the Sierra Madre Occidental. Two new <sup>40</sup>Ar/<sup>39</sup>Ar ages were determined for ignimbrites; 20.4 ± 0.2 Ma (the youngest age obtained so far in this area) and 29.2 ± 0.5 Ma. Density measurements, as a proxy for welding, proved to be extremely useful to estimate the emplacement temperature and the origin of the magnetizations carried by the ignimbrites. After alternating field and thermal demagnetizations, the mean palaeomagnetic pole (Lat = 66.8°N; Long = 180.5°E; Kappa = 142; A<sub>95</sub> = 6.3°), calculated for the period 28–31 Ma, is in close agreement with our only Miocene determination. Comparison with the North America Synthetic Apparent Polar Path indicates a net counter-clockwise vertical axis rotation of about 10 ± 4° compared to stable North America, which occurred likely during the last extensional episode in the Late Miocene (ca. 12–9 Ma). Palaeointensity estimates, obtained with the Thellier–Coe method, are mainly questionable and should not be used for global interpretation. Therefore, these ignimbrites are not a viable material for reliable palaeointensity determinations.

**Key words:** Palaeointensity; Palaeomagnetism applied to tectonics; Rock and mineral magnetism.

### INTRODUCTION AND SAMPLING

Ash flow tuffs or ignimbrites, which often contain magnetic grains with domain states ranging from superparamagnetic to single domain, have been proposed as a potentially good material for palaeointensity determination (Gee *et al.* 2010). However, if the grain size seems to be optimal for that type of analysis, the complex thermal and alteration history during emplacement may lead to magnetizations that are not pure thermoremanent magnetization (TRM), but rather thermochemical remanence (TCRM) or even chemical remanence (CRM) (Draeger *et al.* 2006), and therefore to spurious palaeointensity estimates. As the analysis of Gee *et al.* (2010) on the Bishop Tuff concluded that ignimbrites might constitute a viable material for reliable palaeointensity determinations, a new study was initiated on the Oligo–Miocene ignimbrites from the southern part of the Sierra Madre Occidental (SMO)

in Mexico. In order to have a chance to use the reliability criterion proposed by Biggin *et al.* (2007), which required two distinct types of material both producing some good quality palaeointensity determinations, other rock types (basalts, rhyolites) were also sampled.

From the northern part of the Sierra Los Huicholes, 97 samples were collected in 12 cooling units located between Huejuquilla (Zacatecas) and Estacion Ruiz (Nayarit), as illustrated in Fig. 1. Note that, 6–13 samples were drilled directly at each exposure using a portable gasoline powered drill and oriented *in situ* with both magnetic and sun compasses in most cases. The sampled rocks are mainly rhyolitic ignimbrites, with two basaltic flows and one that is more rhyolitic (Table 1). Except for one site (SMO1) where the volcano–sedimentary sequence is tilted (NE–SW 20°), all other sites are basically flat lying and no tilt correction is necessary.

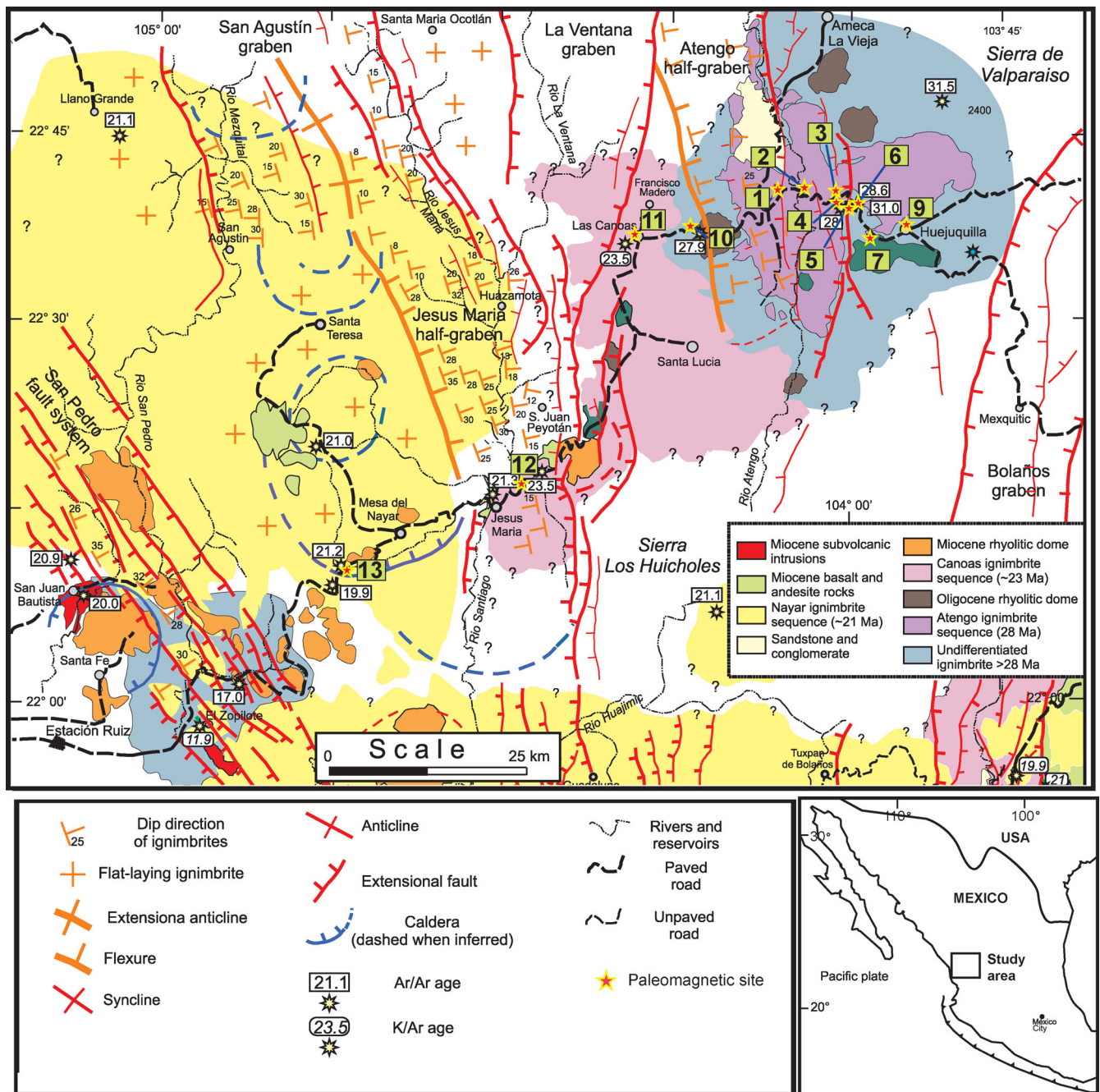


Figure 1. Geologic map of the southern part of the Sierra Madre Occidental with the locations of the palaeomagnetic sites and locations of previous age determinations, modified from Ferrari *et al.* (2002).

**GEOLOGY**

Several reviews have been published on the Sierra Madre Occidental. In 1979, McDowell & Clabaugh (1979) summarized all pioneering studies and gave the first general stratigraphic framework of the SMO. The southern part of the SMO was less well studied than the rest of the province and Nieto-Samaniego *et al.* (1999) were the first to propose a magmatic evolution of the Mesa Central. More recently, Ferrari *et al.* (2002) published a detailed geologic and tectonic framework for this southern area.

The Sierra Madre Occidental resulted from magmatic and tectonic episodes linked to the subduction of the Farallon Plate under

North America and the development of the Gulf of California, between Cretaceous and Cenozoic. Five major igneous complexes are present: (1) Late Cretaceous to Palaeocene plutonic and volcanic rocks; (2) Eocene andesites and lesser rhyolites forming the Lower Volcanic Complex; (3) silicic ignimbrites emplaced during two pulses in the Oligocene and Early Miocene forming the Upper Volcanic Supergroup; (4) transitional basaltic–andesitic lavas erupting after each ignimbrite pulse and (5) alkaline basalts and ignimbrites emplaced after the end of the subduction in Late Miocene, Pliocene, and Pleistocene, which are directly related to the separation of Baja California from the Mexican mainland. These magmatic units cover a heterogeneous basement, Precambrian to Palaeozoic

**Table 1.** Sampling information and palaeomagnetic results. Rock types are respectively IGN for ignimbrite, RHY for rhyolite and BAS for basalt. Ignimbrites units were estimated from the geologic map of Ferrari *et al.* (2002). NI, CI, and AI are respectively for the ~21 Ma Nayar, ~23 Ma Canoa and ~28 Ma Atengo formations; UI marks formations older than 28 Ma. Most ages are from Ferrari *et al.* (2002) and references therein, new ages are indicated by a star.  $N/N_0$  is the number of samples for which a ChRM could be obtained versus the total number of samples.  $D$  and  $I$  are respectively the declination and the inclination of the mean remanence for a given site.  $k$  and  $\alpha_{95}$  ( $K$  and  $A_{95}$ ) are respectively the dispersion parameter and the 95 per cent circle of confidence related to the Fisher statistics for the direction (pole). Chron has been estimated by comparison of the age/polarity with the Ogg & Smith (2004) GPTS. All (Lat, Long) are in decimal degrees.

Site Names	Rock Type	IGN Unit	Age Ma	Site location		Density g/cc	Direction					Chron	Pole					
				Lat °N	Long °W		$N/N_0$	$D$	$I$	$k$	$\alpha_{95}$		Lat°N	Long°E	$K$	$A_{95}$		
SMO1	IGN	AI	20.4		22.67	-104.08	1.8 ± 0.3											
SMO2	IGN	AI	*20.4 ± 0.2		22.67	-104.04	2.3 ± 0.1	1/8	341.3	44.6		C6An.1n	72.6	181.6				
SMO13	IGN	NI	21.2 ± 0.3	Miocene	22.17	-104.72	1.8 ± 0.0											
SMO12	IGN	CI	23.3 ± 0.4		22.29	-104.47	1.8 ± 0.1											
SMO11	IGN	CI	23.3 ± 0.4		22.61	-104.30	2.0 ± 0.1											
SMO10	RHY	-	27.9 ± 0.2		22.63	-104.22	2.5 ± 0.0	8/8	147.9	-40.6	313	3.1	C9r	60.5	172.2			
SMO5	IGN	UI	28.0–28.6		22.66	-103.98	2.4 ± 0.1	7/7	160.6	-51.3	146	5.0	C9r/C10n.1r	70.5	190.6			
SMO3	IGN	AI	28.6 ± 0.3		22.67	-103.99	1.8 ± 0.1											
SMO7	IGN	AI	*29.2 ± 0.5	Oligocene	22.61	-103.94	2.5 ± 0.0	11/13	331.0	45.4	727	1.7	C11n.1n	63.4	181.3			
SMO6	BAS	-	28.6–31.0		22.65	-103.97	2.9 ± 0.0	9/10	342.0	45.7	151	4.2	C11n/C12n	73.1	185.1			
SMO9	BAS	-	31.0		22.63	-103.90	2.2 ± 0.1	7/7	325.9	37.6	194	4.3	C12n	58.4	169.9			
SMO4	IGN	AI	31.0 ± 0.7		22.66	-103.99	2.4 ± 0.0	7/7	163.0	-48.8	642	2.4	C12r	73.2	194.5			
			28–31					6/12	334.6	45.1	118	6.2		66.8	180.5	142	6.3	
			20–31					7/12	335.6	45.1	133	5.3		67.8	180.6	124	5.4	

in age in the northern part (Sonora, Chihuahua) and Mesozoic for the rest of the SMO.

The huge Oligo–Miocene ignimbritic succession of the SMO is one of the largest silicic igneous provinces on Earth, and the largest of the Cenozoic era. It reaches more than 1000 m in thickness and covers most of the western part of Mexico, with an aerial extent of at least 300 000 km<sup>2</sup> (e.g. Ferrari *et al.* 2007), but probably significantly larger. This is the most notable geological feature of the Mexican subcontinent. Another remarkable feature of these silicic deposits is the relatively short time of emplacement. It has been shown that two distinct ignimbritic pulses occurred in the southern region (Ferrari *et al.* 2002). The first and widespread pulse occurred at the beginning of the Oligocene with an impressive synchronicity across the entire province. The second pulse in the Early Miocene was more restricted to the southwestern part of the Sierra Madre Occidental and central Mexico beneath the Trans-Mexican Volcanic Belt. The distribution of this voluminous silicic volcanism defines a clear trend (see fig. 6 in Ferrari *et al.* 2002) with a broad NNW trending Oligocene silicic arc and an ESE migration of this volcanism between the 23–21 Ma pulse. Ignimbrites and rhyolites with <sup>40</sup>Ar/<sup>39</sup>Ar ages (sanidine) between 31.5 and 28 Ma constitute the major part of the Sierra de Valparaiso and the Atengo half graben (Fig. 1). Basaltic lavas emplaced shortly after the Early Oligocene ignimbrites are also exposed around Huejuquilla. The Early Miocene pulse is well expressed in the western part of our studied area.

Large-volume silicic volcanism is characteristic of volcanic arcs undergoing extension or rifting to form backarc basins, and the formation of volcanic rifted margins (Bryan *et al.* 2002). Most of the Sierra Madre Occidental has been affected by different episodes of dominantly extensional deformation starting at the end of the Eocene beginning of Oligocene. Extensional deformation has not affected the core of the Sierra Madre Occidental, which now represents a physiographic boundary between what has been defined as the Mexican Basin and Range to the east and the Gulf Extensional Province to the west (Henry & Aranda-Gómez 2000). At the northern and southern ends of the Sierra Madre Occidental, these two

provinces merge where extension has affected the whole width of the Sierra Madre Occidental. An evolving geographic pattern of this extensional tectonic has been proposed (Ferrari *et al.* 2007) for the SMO from Eocene to Late Miocene. The onset of upper crustal extension seems to follow the first ignimbrite pulse. A second episode affected the central part of the SMO, with an extensional front moving westwards between the Late Oligocene and Early Miocene. In the southern SMO, this extensional episode is expressed by the formation of various grabens with NNE–SSW to N–S orientation between ca. 22 and 18 Ma, and after the beginning of the second ignimbritic pulse at 24–20 Ma. In Late Miocene, a third extensional episode occurred between ca. 12 and 9 Ma.

Ferrari *et al.* (2007) divided the southern part of the Sierra Madre Occidental into three main structural domains (see fig. 9 in Ferrari *et al.* 2007). NNE to NS oriented grabens are the main structures in the eastern domain and cut into Early Miocene ignimbrites (ca. 22–20 Ma). The western domain is characterized by half grabens, as well as normal fault systems with NS to NNW–SSE structures, which systematically tilt blocks of Early Miocene ignimbrites to the ENE. Master faults of the half grabens cut ignimbrites of the El Nayar sequence dated at ca. 21 Ma (Ferrari *et al.* 2002), but no minimum age can be inferred for fault activity. The San Pedro and Pochotitán fault systems were formed by an ENE to NE–SW directed extension and can be considered as part of the Gulf Extensional Province. The Pochotitán fault system tilts rocks as young as 17 Ma, which are covered by flat-lying basaltic lavas dated at ca. 10 Ma (Ferrari & Rosas-Elguera 2000). In this region, many mafic dikes intrude between 11.9 and 10.9 Ma and are associated with NNW normal faults or strike parallel to them (Ferrari *et al.* 2002).

## GEOCHRONOLOGY

Two new <sup>40</sup>Ar/<sup>39</sup>Ar ages were obtained at CICESE's Geochronology Laboratory on ignimbrites from sites SMO2 and SMO7. The argon isotope experiments were conducted on mineral grains with a Coherent Ar-ion Innova 70 laser extraction system on line with a

**Table 2.** Summary of  $^{40}\text{Ar}/^{39}\text{Ar}$  VG5400 laser step heating experiments. Pwr is the laser power applied to release argon in Watts; %  $^{39}\text{Ar}$  is the percentage of  $^{39}\text{Ar}$  released;  $^{40}\text{Ar}_r/^{39}\text{Ar}_K$  is the ratio of the radiogenic  $^{40}\text{Ar}$  to the potassium derived  $^{39}\text{Ar}$ ;  $t$  is the age of individual fraction (does not include the uncertainty in  $J$ ); %  $^{40}\text{Ar}$  is the percentage of radiogenic  $^{40}\text{Ar}$ ;  $^{37}\text{Ar}_{\text{Ca}}/^{39}\text{Ar}_K$  is the ratio of calcium derived  $^{37}\text{Ar}$  to potassium derived  $^{39}\text{Ar}$ ;  $t_i$ ,  $t_p$  and  $t_c$  are respectively the integrated age, the plateau age calculated with the weighted mean of the fractions identified with the '§' symbol, and the isochron age (fractions ignored to calculate the isochron age are identified with the '†' symbol);  $(^{40}\text{Ar}/^{36}\text{Ar})_i$  is the initial ratio  $^{40}\text{Ar}/^{36}\text{Ar}$ ; MSWD is the goodness of fit parameter of the best straight line and  $n$  is the number of points used to calculate the straight line; '†' fractions ignored in the isochron age calculation; all errors are given to  $1\sigma$  level. The irradiation parameter  $J$  for the samples is  $0.002993 \pm 0.000044$ . Preferred ages are highlighted in bold.

	Pwr	% $^{39}\text{Ar}$	$^{40}\text{Ar}_r/^{39}\text{Ar}_K$	$t$ (Ma)	% $^{40}\text{Ar}$	$^{40}\text{Ar}/^{36}\text{Ar}$	$^{37}\text{Ar}_{\text{Ca}}/^{39}\text{Ar}_K$	$t_i$ (Ma)	$t_p$ (Ma)	$t_c$ (Ma)	$(^{40}\text{Ar}/^{36}\text{Ar})_i$	MSWD/ $n$
SMO-03	0.20	1.86	$17.90 \pm 1.24$	$94.1 \pm 6.4$ †	12.79	338.82	0.015	$21.9 \pm 0.4$	<b><math>20.4 \pm 0.2</math></b>	$20.4 \pm 0.4$	$299 \pm 9$	5.9 / 6
	0.40	13.50	$3.51 \pm 0.04$	$18.8 \pm 0.2$ †	49.79	588.50	0.009					
	0.60	21.27	$3.77 \pm 0.04$	$20.2 \pm 0.2$ §	86.37	2168.24	0.008					
	0.90	20.88	$3.86 \pm 0.04$	$20.7 \pm 0.2$ §	92.38	3879.26	0.008					
	1.30	12.32	$3.79 \pm 0.03$	$20.4 \pm 0.2$ §	92.63	4012.21	0.009					
	2.00	10.47	$3.76 \pm 0.04$	$20.2 \pm 0.2$ §	77.06	1288.36	0.008					
	3.00	17.10	$4.13 \pm 0.07$	$22.2 \pm 0.4$	61.94	776.50	0.009					
	6.00	2.60	$3.78 \pm 0.15$	$20.3 \pm 0.8$	20.33	370.91	0.017					
	3.00	13.68	$5.82 \pm 0.59$	$31.1 \pm 3.1$ §	51.54	609.76	0.032	$29.8 \pm 1.2$	$29.4 \pm 0.4$	<b><math>29.2 \pm 0.5</math></b>	$313 \pm 10$	7.7 / 7
	4.50	8.07	$5.38 \pm 0.21$	$28.8 \pm 1.1$ §	84.52	1908.84	0.031					
5.50	13.87	$5.45 \pm 0.16$	$29.2 \pm 0.8$ §	92.07	3725.18	0.033						
SMO-07	6.00	6.95	$5.32 \pm 0.15$	$28.5 \pm 0.8$ §	94.16	5055.79	0.036					
	6.50	21.95	$5.62 \pm 0.15$	$30.1 \pm 0.8$ §	96.94	9642.20	0.034					
	7.00	11.99	$5.48 \pm 0.15$	$29.4 \pm 0.8$ §	98.09	15494.34	0.028					
	7.50	23.50	$5.62 \pm 0.14$	$30.1 \pm 0.7$ §	97.79	13347.45	0.036					

VG5400 mass spectrometer. The samples and irradiation monitors, aliquots of sanidine TCR-2 ( $27.87 \pm 0.04$  Ma) and FCT-2 ( $27.84 \pm 0.04$  Ma), were irradiated in the U-enriched research reactor of McMaster University in Hamilton (Canada) at position 5C in capsule CIC-58 for 10 hr. To block thermal neutrons, the capsule was covered with a cadmium liner during irradiation. The irradiation monitors were distributed evenly among the samples to minimize the effect of neutron flux variations. Upon irradiation the monitors were fused in one step, the measured  $^{40}\text{Ar}_r/^{39}\text{Ar}_K$  was used to determine  $J$ , the irradiation parameter. The samples were step heated by increasing the laser power applied. The argon isotopes were corrected for blank, mass discrimination, radioactive decay of  $^{37}\text{Ar}$  and  $^{39}\text{Ar}$  and atmospheric contamination. For the Ca neutron interference reactions, the factors given by Masliwec (1984) were used. The decay constants recommended by Steiger & Jäger (1977) were applied in the data processing. The equations reported by York *et al.* (2004) were used in all the straight line fitting routines of the argon data reduction.

For each sample, relevant  $^{40}\text{Ar}$ – $^{39}\text{Ar}$  data is presented in Table 2, it includes the results for individual steps, integrated, plateau and isochron ages, and the preferred age highlighted in bold. Age spectra,  $^{37}\text{Ar}_{\text{Ca}}/^{39}\text{Ar}_K$  diagrams and  $^{36}\text{Ar}/^{40}\text{Ar}$  versus  $^{39}\text{Ar}/^{40}\text{Ar}$  correlation diagrams are presented in Fig. 2. The plateau age was calculated from the weighted mean of three consecutive fractions that have individual ages in agreement within  $1\sigma$ , and more than 30 per cent of the  $^{39}\text{Ar}$  released in the plateau segment. The analytical precision is reported as one standard deviation ( $1\sigma$ ). The fractions that fulfill the criteria for plateau age calculation are identified in Table 2 with the '§' symbol and by an arrow in Fig. 2. The argon isotopic data obtained were plotted in the  $^{36}\text{Ar}/^{40}\text{Ar}$  versus  $^{39}\text{Ar}/^{40}\text{Ar}$  correlation diagram. The isochron age is calculated from the  $x$ -intercept of the best straight line defined. In Table 2, the fractions not used to calculate the isochron age are identified with the '†' symbol. The analytical precision is also reported as one standard deviation ( $1\sigma$ ). The errors in the plateau, integrated and isochron ages include the uncertainty in  $J$ , the irradiation monitor.

For sample SMO7, a few grains of sanidine were step heated; the argon isotopes yielded statistically indistinguishable ages for

the individual fractions. However, a subtle saddle shape can be observed in the age spectrum (see Fig. 2 and Table 2). The best straight line defined by all individual fractions collected gave a ratio  $(^{40}\text{Ar}/^{36}\text{Ar})_i$  of  $313 \pm 10$  Ma. Since  $(^{40}\text{Ar}/^{36}\text{Ar})_i > 295.5$  Ma suggests the presence of excess argon, the isochron age of  $29.2 \pm 0.5$  Ma is preferred over the plateau age.

For sample SMO2, a few fragments of a groundmass concentrate were laser step heated. A disturbed age spectrum can be seen with a saddle shaped age spectrum superimposed over an argon loss shaped spectrum (Fig. 2). However, four central fractions yield a reliable plateau age of  $20.4 \pm 0.2$  Ma, representing about 65 per cent of the  $^{39}\text{Ar}$  released. With the exception of two fractions released with a laser power less than 0.5 Watts, the data define an isochron age of  $20.4 \pm 0.4$  Ma. This less precise age is indistinguishable from the plateau age, which we take as the best estimate for that site. Site SMO2, which is located at the top of the ignimbritic sequence, has therefore the youngest age reported so far.

## PALAEOMAGNETIC DATA

Laboratory analyses were conducted in the palaeomagnetic laboratories of Geosciences Montpellier (GM) and Universidad Nacional Autonoma de Mexico (UNAM). Samples were cut into one to three cylindrical specimens of regular size (2.5 cm in diameter and 2.2 cm in height). Remanent magnetization of the samples was measured either with the Montpellier 2G Enterprises cryogenic magnetometer coupled with an automated sample handler and located in a magnetically shielded room, or with the UNAM JR5 spinner magnetometer.

Pilot specimens were progressively demagnetized using an alternating field (AF) unit inline with the GM cryogenic, using around 20 steps up to the maximum field, which can be applied (170 mT). Detailed stepwise thermal demagnetization up to 680 °C was also carried out on one pilot-sample per flow using the UNAM non-inductive Schonstedt furnace. Similar results were obtained from thermal and AF demagnetizations, although surprisingly thermal demagnetizations were a lot noisier than AF ones. Therefore, all other samples were treated by AF demagnetization with 10–15 steps

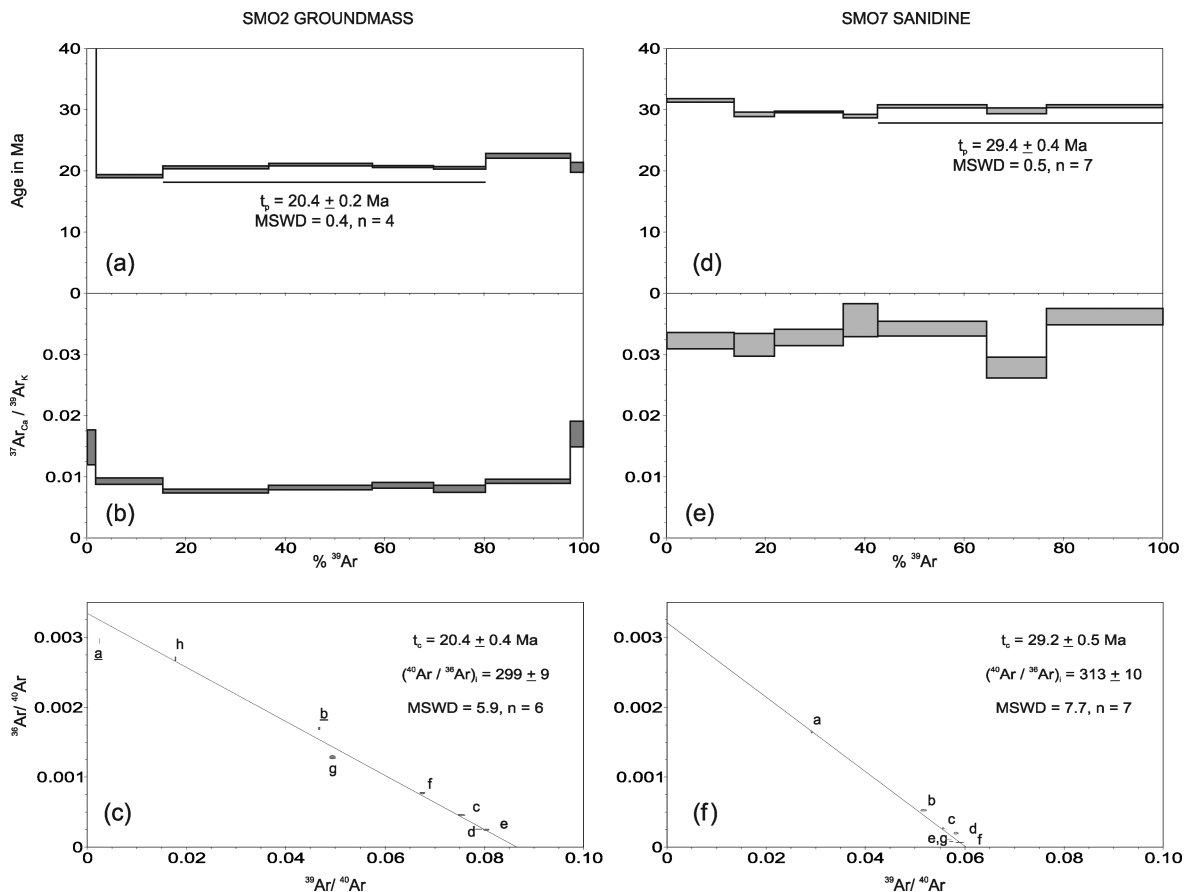


**Figure 2.** Age spectra and isochron correlation diagrams for samples SMO2 groundmass (a, b, c) and SMO7 sanidine (d, e, f).  $t_p$  is the plateau age, obtained with the weighted mean of the fractions identified with the arrow. MSWD is the goodness of fit of the weighted mean and  $n$  is the number of fractions used.  $t_c$  is the isochron age calculated with the best straight line defined by the data points selected. The sequence of letters in the <sup>36</sup>Ar/<sup>40</sup>Ar versus <sup>39</sup>Ar/<sup>40</sup>Ar correlation diagrams identifies the order of the fractions from the step-heating experiment. The underlined letters identify the fractions not used in the isochron age calculation. MSWD is the goodness of fit of the straight line and  $n$  is the number of point used.

depending on the coercivity of the samples. Principal component analysis PCA (Kirsink 1980) was used to estimate the direction of Characteristic Remanent Magnetizations (ChRMs). Maximum angular deviation (MAD) measured in the PCA was less than 4° for most determinations. Palaeomagnetic plots were prepared with Lisa Tauxe's PmagPy 2.51 software package (Tauxe 2010).

No mean direction of magnetization could be obtained from three Miocene ignimbritic sites (SMO1, SMO11 and SMO12) and one Oligocene site (SMO3), either because no ChRM could be estimated for individual samples or because only very poorly defined means could be calculated. These ignimbrites are characterized by very low coercivity magnetic minerals (40–90 per cent of the magnetization removed by 5–20 mT).

On the other hand, very high coercivity magnetic minerals (less than 20 per cent of the magnetization is destroyed by 170 mT, with most magnetization removed only between 650–680 °C, Figs 3a and b) characterized the Miocene ignimbritic site (SMO13), likely fine-grained hematite. The mean site direction (Dec = 359.1°; Inc = 33.1°; kappa = 1520;  $\alpha_{95}$  = 3.2) indicates a total remagnetization of these samples in a recent field (Geocentric Axial Dipole inclination is 39° at the site latitude, Fig. 3c).

The last Miocene ignimbritic site (SMO2) is characterized by some samples that have extremely high NRM intensities, median destructive fields of around 10 mT, and directions of magnetization that are well defined, but variable from sample to sample. This is characteristic of isothermal remanent magnetization (IRM) ac-

quired during lightning strikes. Site SMO2, the youngest ignimbrite we could sample, forms a small peak, which is a situation prone to lightning strikes. However, all samples were not remagnetized the same way, as indicated by the NRM intensities (see variations in NRM intensity, Fig. 4). Some samples were completely remagnetized (Fig. 4a), others only partially (Fig. 4b), and finally one sample (Fig. 4c) was not disturbed and presents a ChRM comparable to the normal polarity of the rest of the samples. This is our only palaeomagnetic result for the Miocene.

All other Oligocene sites presented well-defined magnetizations after removal of a small viscous component by 5–10 mT. Most samples contain two different magnetic carriers as illustrated by the thermal demagnetization curves (Figs 5, 6 and 7), but only one component of magnetization (see orthogonal diagrams of Figs 5, 6 and 7). However, the fraction of the high coercivity mineral, likely hematite, is variable and depends on the samples: 9–83 per cent of the magnetization left after 170 mT for the rhyolites (Fig. 5), 1–68 per cent for the ignimbrites (Fig. 6) and 22–81 per cent for the basalts (Fig. 7).

Individual directions of magnetization were averaged per site and statistical parameters calculated assuming a Fisherian distribution. The two basaltic sites (SMO6 and SMO9), one of the Oligocene ignimbritic sites (SMO7) and the one sample from the Miocene site (SMO2) are normally magnetized while the rhyolitic site SMO10 and the two other Oligocene ignimbritic sites (SMO4 and SMO5) present a reversed polarity (Fig. 8, Table 1). Both normal and

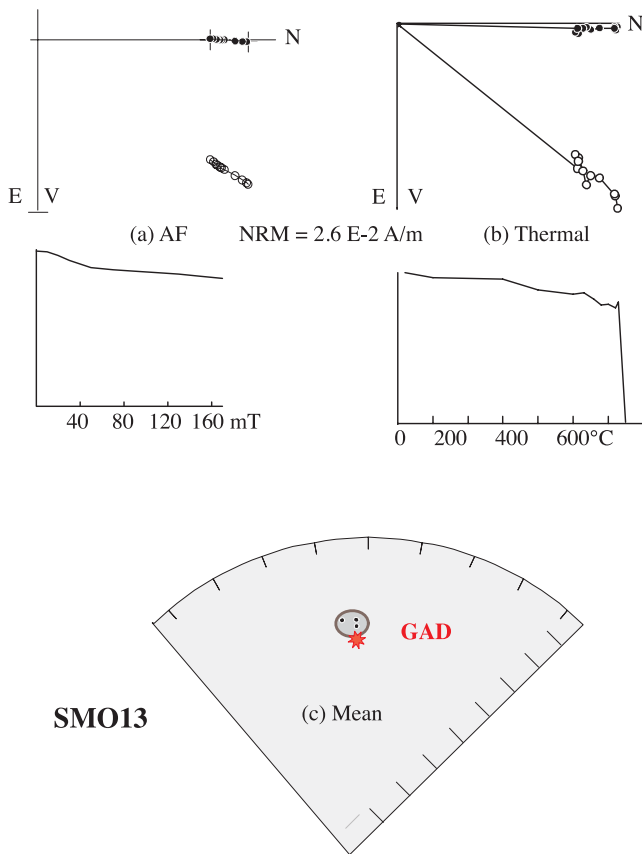


**Figure 3.** Comparison between AF (a) and thermal (b) demagnetizations for an SMO13 sample. Full (open) circles are projections onto the horizontal (vertical) planes of the orthogonal diagrams, subpart (c) compares the SMO13 ChRMs and the present geomagnetic axial dipole GAD.

reversed directions were independently averaged and the reversal test of McFadden & McElhinny (1990) was applied. The angle between mean normal and reversed polarity directions is  $3.6^\circ$  and passes the reversal test. Therefore, a SMO mean palaeomagnetic direction (Table 1) was calculated with the Oligocene (28–31 Ma) sites ( $N = 6$ ; Dec =  $334.6^\circ$ ; Inc =  $45.1^\circ$ ; kappa = 118;  $\alpha_{95} =$

$6.2^\circ$ ), which corresponds to a virtual geomagnetic pole VGP (Lat =  $66.8^\circ\text{N}$ ; Long =  $180.5^\circ\text{E}$ ; Kappa = 142;  $A_{95} = 6.3^\circ$ ). If the single result obtained from SMO2 samples is taken into account, the mean direction remains basically the same ( $N = 7$ ; Dec =  $335.6^\circ$ ; Inc =  $45.1^\circ$ ; Table 1), but the time interval would be much larger covering the Oligo–Miocene (20–31 Ma). More data will be necessary to support this hypothesis.

### ROCK MAGNETIC ANALYSIS

A detailed microscopic analysis has been carried out on the Sierra Madre Occidental samples (Alva-Valdivia *et al.* submitted), using both reflected and transmitted lights. Results of interest for our palaeomagnetic analysis are summarized below.

(1) *Andesitic basalt flows (sites SMO6 and SMO9)*. The grain sizes of the SMO6 oxides (Fig. 9a) are larger than those of SMO9 basalt, but the degree of oxidation is lower. The SMO6 basalt contains 12 per cent of Fe–Ti oxides (matrix and rock fragments). Its matrix is formed mainly by titanomaghemites (5–25  $\mu\text{m}$ ) forming columnar shapes ( $<132 \mu\text{m}$ ) cutting the plagioclases in distinct trends, and surrounding the phenocrystals (Fig. 9a). The SMO9 andesitic basalt has experienced strong hydrothermal oxidation of the mineral oxides, as indicated by some occurrence of goethite. Abundant Fe–Ti altered oxide grains are occupying free spaces between plagioclase (hematite, 0.2–15  $\mu\text{m}$  and titanomagnetite, 0.5–60  $\mu\text{m}$ , Fig. 9b).

(2) *Microcrystallized rhyolitic ignimbrites (sites SMO4, SMO5, SMO7 and SMO13)*. Rock fragments are ochre red in color due to their high content in Fe–Ti oxide inclusions disseminated homogeneously. In sites SMO4, SMO5 and SMO7, the rock fragments are scarce and small ( $<1 \text{ mm}$ ) compared to site SMO13 (maximum grain size 5 mm). The microcrystallized rhyolitic tuffs have distinct alteration of their Fe–Ti oxide minerals, with titanomagnetite partly altered to titanohematite. The degree of oxidation is decreasing from sites SMO7, SMO13, SMO5, to SMO4 (Fig. 9c).

(3) *Rhyolitic ignimbrite welded tuff (sites SMO3, SMO12 and SMO11)*. The texture is clastic (22 per cent of Fe–Ti oxide fragments) with a volcanic glass matrix. The devitrification degree of the volcanic glass and the alteration degree of feldspar decrease from

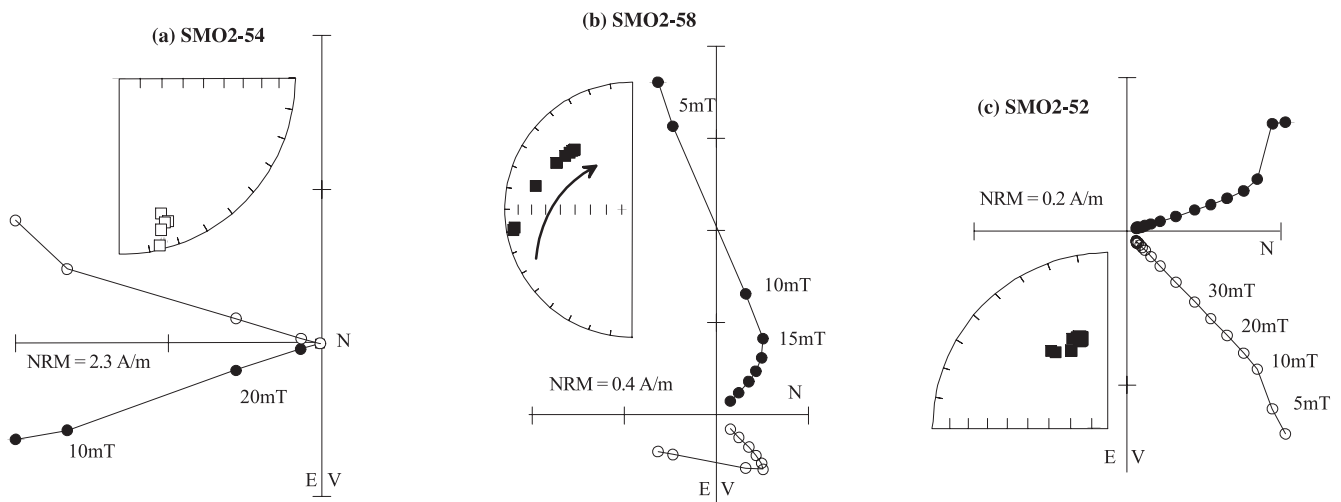


**Figure 4.** Representative AF demagnetizations for SMO2 ignimbritic samples. Subparts (a), (b), (c) are, respectively, the examples of total, partial and no remagnetization by IRM. Full (open) circles are, respectively, projections onto the horizontal (vertical) planes of the orthogonal diagrams. Full (open) squares are positive (negative) inclinations on the equal area plots.

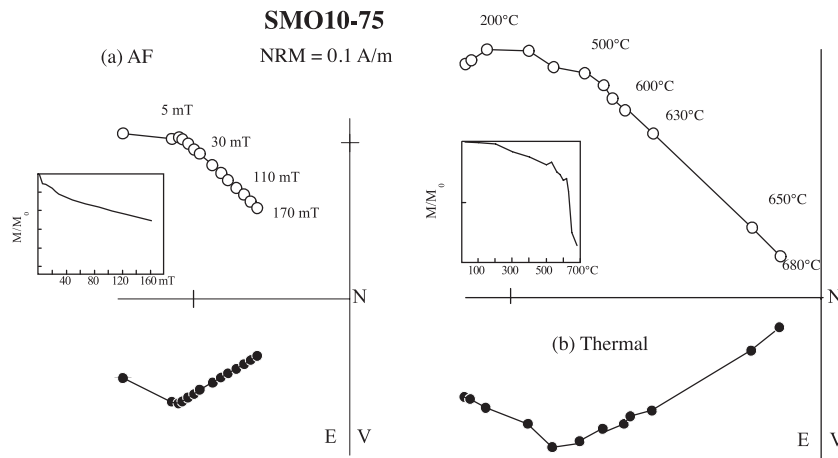


**Figure 5.** Comparison between AF (a) and thermal (b) demagnetizations for a rhyolitic sample of site SMO10. Full (open) circles are projections onto the horizontal (vertical) planes of the orthogonal diagrams.

sites SMO3, SMO12 to SMO11 (Fig. 9d). Sites SMO3 and SMO12 contain mainly anhedral disseminated titanomagnetite crystals (2–100  $\mu\text{m}$ ), occasionally forming a mixture of particles with titanohematite. In site SMO11, small crystals of titanohematite (2–28  $\mu\text{m}$ , Fig. 9d) are dominant.

(4) *Vitreous acid tuff (site SMO1)*. These samples have a clastic texture (45 per cent) comprised of several translucent minerals, Fe–Ti oxides and scarce rock fragments partly silicified against a volcanic glass (55 per cent), which forms the rock matrix. Scarce, isolated titanomagnetite anhedral crystals (2–40  $\mu\text{m}$ ) with skeletal texture are present and partly altered to titanohematite along their borders (Fig. 9e).

(5) *Silicified potassic rhyolitic flow with a porphyric texture (site SMO10)*. Fe–Ti oxide minerals are estimated at 2 per cent. Granular and semi-octahedral titanohematite crystals (5–200  $\mu\text{m}$ ) are homogeneously distributed (Fig. 9f). In general, silicification is the result of hydrothermalism and substitution of the original rock by silica that can be quartz or microcrystalline silica, or both.

(6) *Silicified rock (site SMO2)*. Samples from this unit, emplaced as an ignimbrite, have a fine granular texture formed by irregular quartz grains up to 120  $\mu\text{m}$  in size (20  $\mu\text{m}$  average), intergrown with microcrystalline silica, which fills the open spaces and veins of the rock, and is probably syngenetic. Anhedral and semi-octahedral titanohematite crystals (2–12  $\mu\text{m}$ ) form a skeletal texture with pseudo-brookite lamellae relicts.

Isothermal remanence (IRM) acquisition curves were measured for all sites with the UNAM homemade pulse magnetizer, which can reach 3T. All sites, from which no mean site directions could be obtained, have very low coercivities and plot on the left-hand side of the diagram (dotted lines, Fig. 10). Sites SMO1, SMO2 and SMO3 are characterized by magnetic minerals that saturate in low fields (500 mT), likely (Ti) maghemite, while sites SMO11 and SMO12 present two magnetic phases, a first one that saturates also by 500 mT and second phase that saturates only by 2–3 T, likely (Ti) hematite. For site SMO13 (dashed line, Fig. 10), remagnetized in a recent field, the second high coercivity phase is clearly evident. All sites from which a mean direction was obtained (solid lines, Fig. 10) do not saturate before 3T, which indicates the presence of hematite. No difference can be seen between reverse and normal polarity samples.

One sample from each site was further studied using an AGFM Micromag apparatus in fields up to 1.5 Tesla, which provides hysteresis curves, direct field IRM acquisition and back-field curves from microsamples. Near the origin, most of the hysteresis plots have pot-bellied (SMO11) or wasp-waisted (SMO4 and SMO13) behaviour (Fig. 11). These distorted loops were proposed to result from a mixture of several magnetic phases and/or domain states (Wasilewski 1973; Roberts *et al.* 1995; Tauxe *et al.* 1996). The only exception is site SMO6, with hysteresis loops that would generally be interpreted to indicate a dominance of pseudo-single domain (PSD) grains. The saturation remanent magnetization ( $M_{rs}$ ), saturation magnetization ( $M_s$ ) and coercive force ( $H_c$ ) can be calculated from the hysteresis curves, after correction for the paramagnetic contribution, and the coercivity of remanence ( $H_{cr}$ ) estimated from IRM acquisition and back-field curves. In the case of magnetite, the ratios  $M_s/M_{rs}$  as a function of  $H_{cr}/H_c$  give an indication of the magnetic minerals grain size (Day *et al.* 1977). Most of our samples presenting a mixture of magnetite, maghemite and hematite, no grain size inference can be made based on that method.

The thermal stability of the samples has been tested for all sites that yield a mean direction of magnetization, as an *a priori* selection criterion for palaeointensity experiments. Thermomagnetic curves of low-field susceptibility versus temperature were measured in Argon atmosphere using the GM kappabridge susceptibility meter. Two cycles were applied: a first cycle was made by heating from room temperature RT up to 320  $^{\circ}\text{C}$ , followed by cooling back to RT; the second cycle going from RT to 610  $^{\circ}\text{C}$  and back. Ignimbrites from sites SMO4 and SMO5 have low initial susceptibility (Figs 12a and b), but very stable thermomagnetic curves with a Curie temperature around 580  $^{\circ}\text{C}$ . However, hysteresis measurements (SMO4, Fig. 11) indicate a two-phase mixture. Likely the magnetite fraction dominates in the low-field measurements, while the high-coercivity mineral (likely hematite) dominates in the strong-field hysteresis measurements. During the first cycle, SMO7 ignimbrite (Fig. 12c) behaves similarly but the second cycle induces the formation of a much more susceptible phase, likely magnetite resulting from hematite reduction, as previously reported (Hoffman *et al.* 2008). It is worth noting that clay minerals, common hydrothermal alteration products that could be seen during the microscopy investigation, can also act as a catalyst for hematite reduction (Zhang *et al.* 2012). SMO10 rhyolite and SMO6 basalt (Figs 12d and e) are characterized by reversible curves up to 320  $^{\circ}\text{C}$ , but irreversible above, with the

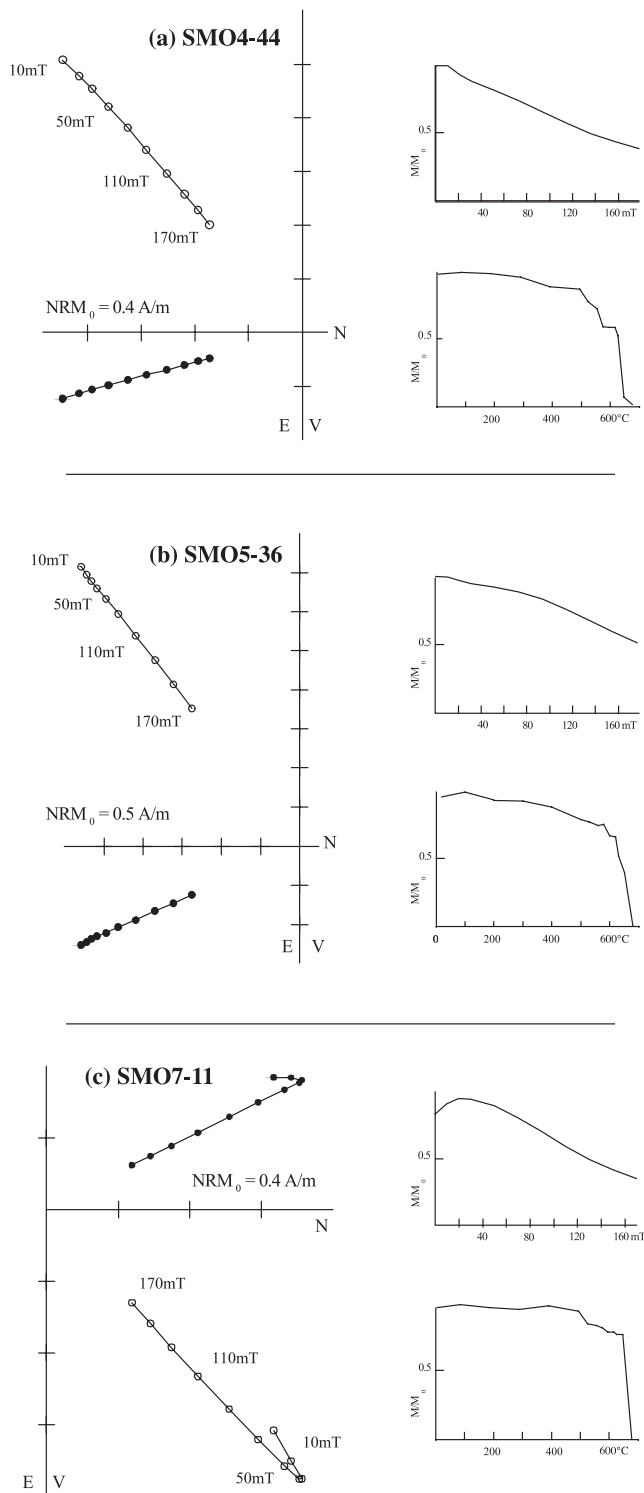


**Figure 6.** Representative demagnetization diagrams (AF orthogonal plot and AF and thermal demagnetization curves) for ignimbrites. Full (open) circles are projections onto the horizontal (vertical) planes.

formation of a less susceptible mineral, likely titanomaghemite altered by oxidation during heating to titanohematite. Finally, SMO9 basalt (Fig. 12f) is characterized by an inflection in the heating curve of the second cycle around 400 °C followed by an irreversibility, which may indicate a mixture of titanomagnetite and titanomaghemite.

**PALAEOINTENSITY**

Palaeointensity experiments were performed at UNAM on 47 samples from the six sites with site mean directions. The Thellier method as modified by Coe was applied (Thellier & Thellier 1959; Coe 1967). For each temperature step, demagnetization of the natural remanent magnetization (NRM) in zero field was followed by acquisition of a partial TRM pTRM in a 30- $\mu$ T laboratory field. Temperatures ranged from 200 to 500 °C with 50 °C steps and from 500 to 640 °C with 20 °C steps. Stability of the pTRM acquisition capacity was checked using the sliding pTRM checks method proposed by Prévot *et al.* (1985) after each second heating step.

The ThellierTool 4.22 software (Leonhardt *et al.* 2004) was used to estimate the linear segment on the Arai plot and the determinations were classified in three groups A, B and C, following all criteria defined by Leonhardt *et al.* (2004) about the linearity of the diagram and the fraction of magnetization used in the calculation, the quality of the demagnetization, and the reproducibility of the pTRM checks. Slight modifications were introduced in the limits used for class B, with slightly less stringent criteria for the NRM fraction ( $N = 3$  and  $f = 0.2$  instead of 5 and 0.3) but stricter one about the direction ( $MAD = 10$  instead of 15). The software automatically calculates the linear segment that best fulfills the above criteria. A linear segment was thus defined on the Arai plots for 22 of the 47 measured samples with supposedly good technical quality.

Half of the basaltic flow samples have a linear segment on the Arai plot for which a palaeointensity could be calculated (Table 3). The mean site value ( $45.2 \pm 2.0 \mu\text{T}$ ), defined from SMO6 samples in the middle temperature range, is well grouped ( $\pm 4$  per cent) and similar to the present-day field intensity. In one case (SMO6-24), the palaeointensity defined by automatic calculation (Fig. 13) corresponds to a higher unblocking range (540–640 °C) with a lower estimate. We preferred to choose the 200–560 °C interval, which corresponds to the same magnetic carrier as for the other samples, and favour the internal consistency criterion, even though the rank lowers from B to C because of the alteration criteria. The nature of the magnetization carried by these rocks is not straightforward. Thermomagnetic curves (Fig. 12e) indicate the formation of a less susceptible mineral, likely (titano)maghemite altered by oxidation during heating to (titano)hematite, at a temperature higher than the upper limit of the first cycle (300 °C). A TCRM or even a CRM was likely acquired during this alteration. This would have no obvious effect on the directional analysis if it happens shortly after emplacement of the basalt, but the palaeointensity estimate would be affected, even without a clear departure of the linearity of the Arai plot (see for example Draeger *et al.* 2006; Fabian 2009). However, one would expect that the effect on the palaeointensity estimate will be dependent on the degree of TCRM formation, which should not be the same for all samples, and will therefore introduce scatter within the estimates at the site level. The high internal consistency ( $\pm 4$  per cent) of results from that site tends to indicate that the palaeointensities were estimated before alteration, when the magnetization was a TRM. SMO9 samples also give technically good palaeointensity estimates (Table 3, Fig. 13), but the mean value ( $28.5 \pm 7.3 \mu\text{T}$ ) is much lower and the dispersion much higher ( $\pm 25$  per cent). The magnetic properties of these samples are very similar to SMO6 samples, and this higher dispersion is likely to reflect the influence of TCRM.

All samples from the rhyolitic flow site SMO10 are characterized by an acquisition of TRM twice the NRM intensity. Linear segments on the Arai plots were automatically estimated for most samples; the palaeointensity values thus calculated are obviously very low

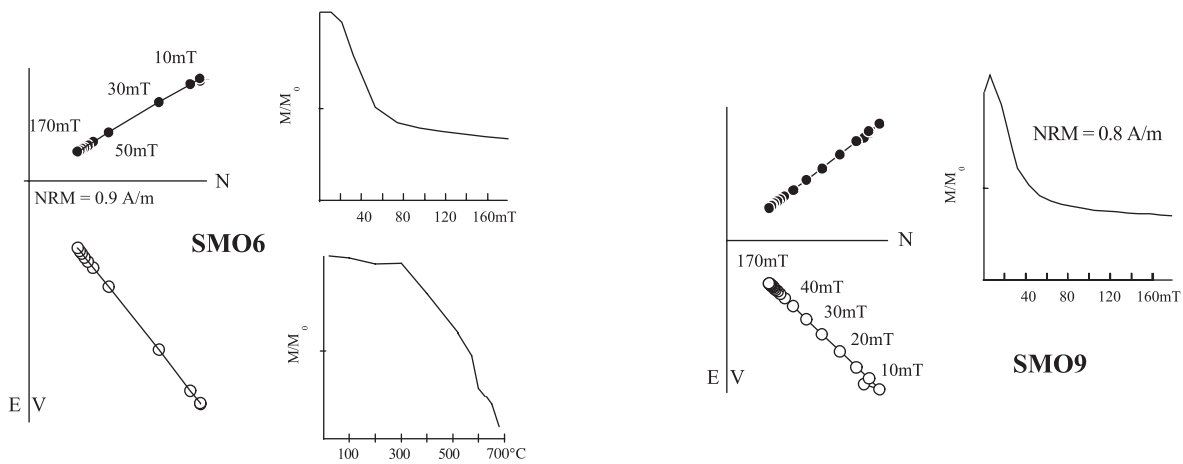


**Figure 7.** Representative AF demagnetization diagrams (orthogonal plot and demagnetization curve) for basaltic samples. Full (open) circles are projections onto the horizontal (vertical) plans.

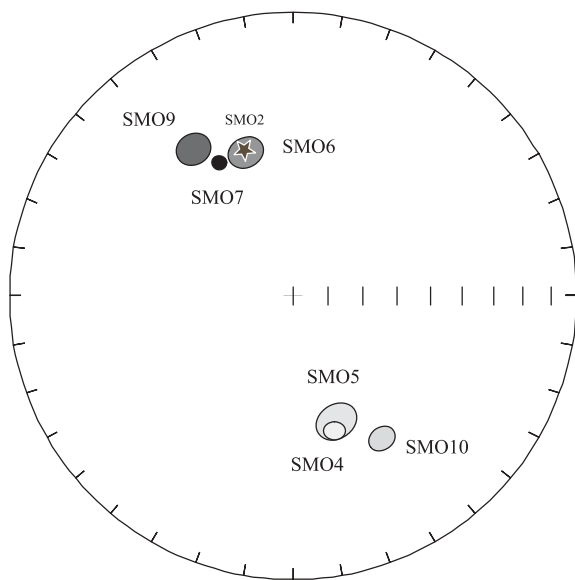


**Figure 8.** Equal area plot of the mean palaeomagnetic directions with their  $\alpha_{95}$  circles of confidence. Full (open) symbols are projections onto the upper (lower) hemisphere. The star indicates SMO2.

( $7.5 \pm 3.0 \mu\text{T}$ ) and dispersed (40 per cent, Table 3). Looking at the Arai plots, a change in the slope is apparent (Fig. 14a) that could be related to the presence of two magnetic phases or components, or a mixture of MD grain size or both. Furthermore, the orthogonal diagrams obtained through palaeointensity experiments show two or even three components of magnetization overlapping through the entire demagnetization range. AF and thermal demagnetization done for these samples (Fig. 5) also show a secondary component but removed by 5 mT or 300 °C, likely a viscous remanent magnetization. The overlap that persists in the high temperature range during the palaeointensity experiment suggests the occurrence of some alteration during heating, not seen in zero field. Finally, when the palaeointensity is estimated within a different temperature interval (200 to 400–540 °C) for which the NRM fraction is too small to fulfill the chosen selection criteria, the mean value is even more scattered, but also much higher ( $37.6 \pm 21.8 \mu\text{T}$ ). For all these reasons, we suspect an underestimation of these determinations made

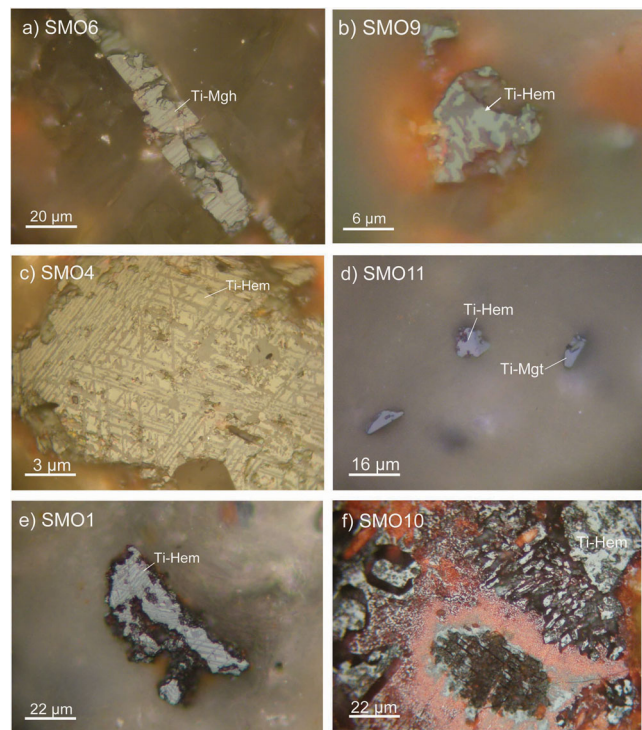


**Figure 9.** Microphotographs of representative oxide minerals. Ti-Mgt, titanomagnetite; Ti-Mgh, titanomaghemite; Ti-Hem, titanohematite; Psb, pseudo-brookite; Goe, goethite.

in the middle to high temperature range and would strongly advise against using them for global interpretation.

Most ignimbric samples yield fairly similar magnetic characteristics: only one component of magnetization, a prominent hematitic component (usually less than 50 per cent of the NRM is demagnetized by 600 °C), little alteration during heating (see pTRM checks in Fig. 14) as also indicated by the reversible  $K/T$  plots of SMO4 and SMO5 (Fig. 12). The main difference is in the capacity of acquisition of the TRM, which is extremely variable and leads to palaeointensity estimates either extremely high for SMO4 and SMO5 (ranging from 64 to 112  $\mu\text{T}$ , Table 3) or very low for SMO7 (7  $\mu\text{T}$ , Table 3). The dispersion around the mean values for sites SMO5

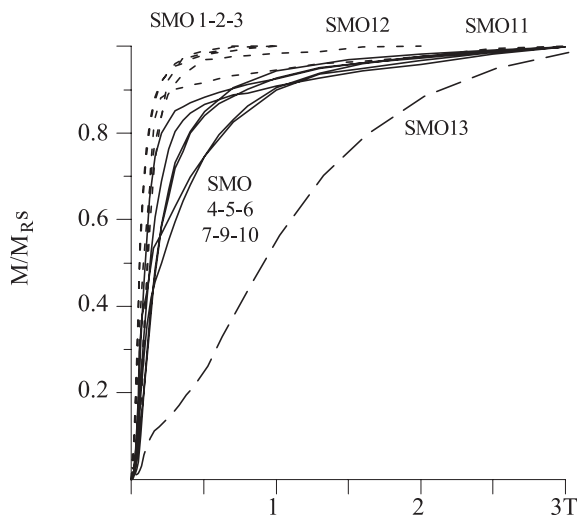


**Figure 10.** Isothermal Remanent Magnetization acquisition curves. Solid (dashed) lines are, respectively, for samples for which a ChRM could (could not) be defined.

and SMO4 is respectively 14 and 13 per cent, which are relatively good within site consistencies. Furthermore, some of the determinations with extremely high values have also extremely good statistical parameters (e.g. SMO4-40, with a palaeointensity of  $112.3 \pm 3.6 \mu\text{T}$  and a  $q$  value of 17, Fig. 14b). However, Fabian (2009) suggests that a TCRM could produce high quality statistics, while yielding high intensity estimates. This is also supported by the experimental work of Draeger *et al.* (2006) although the intensity

overestimate is not as high as predicted by Fabian. Therefore, the high values for SMO5 and SMO4 are questionable. For the very low estimate of site SMO7, the grains that carry the remanence have blocking/unblocking temperatures (450–640 °C) that overlap the temperatures of mineralogical alteration (see Fig. 12c). This observation, combined with the lack of within site consistency, allows the rejection of the mean result for SMO7.

**DISCUSSION**

The emplacement temperature is one of the most critical factors to evaluate the nature of the remanence in the ignimbrites. The most densely welded rocks, emplaced close to the source, are considered to have been formed at temperatures approaching the liquidus (~700 to 900 °C) and will therefore likely carry a pure thermal remanent magnetization TRM. However, more distal deposits, or flows with significant mixing with air, may have been emplaced at considerably lower temperatures and could easily carry a TCRM instead of a TRM, especially considering the magnetic mineralogy of our samples. As emplacement temperatures are not available for our rocks, densities have been estimated for all sites. Qualitative estimates can then be done by analogy to thermal modelling results because, in a single cooling unit, the maximum density and the thickness of the zone of partial compaction both increase as either the temperature or initial thickness increase (Riehle *et al.* 1995). All sites for which we could estimate a mean direction of magnetization have bulk densities between 2200 and 2900 kg m<sup>-3</sup> (squares in Fig. 15); the lowest and the highest densities corresponding to the two basaltic sites. The thermal modelling of Riehle *et al.* (1995) suggests that, for a simple cooling unit, such high densities

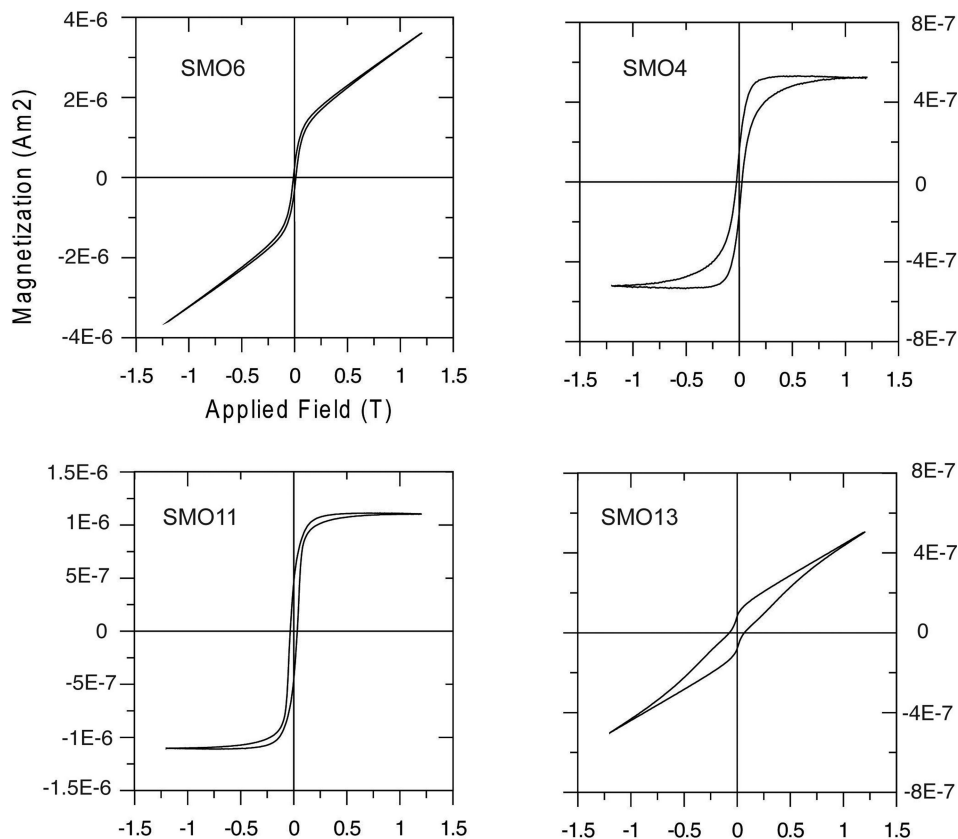


**Figure 11.** Hysteresis loops without paramagnetic correction respectively for SMO6 basalt, SMO4, SMO11 and SMO13 ignimbrites.

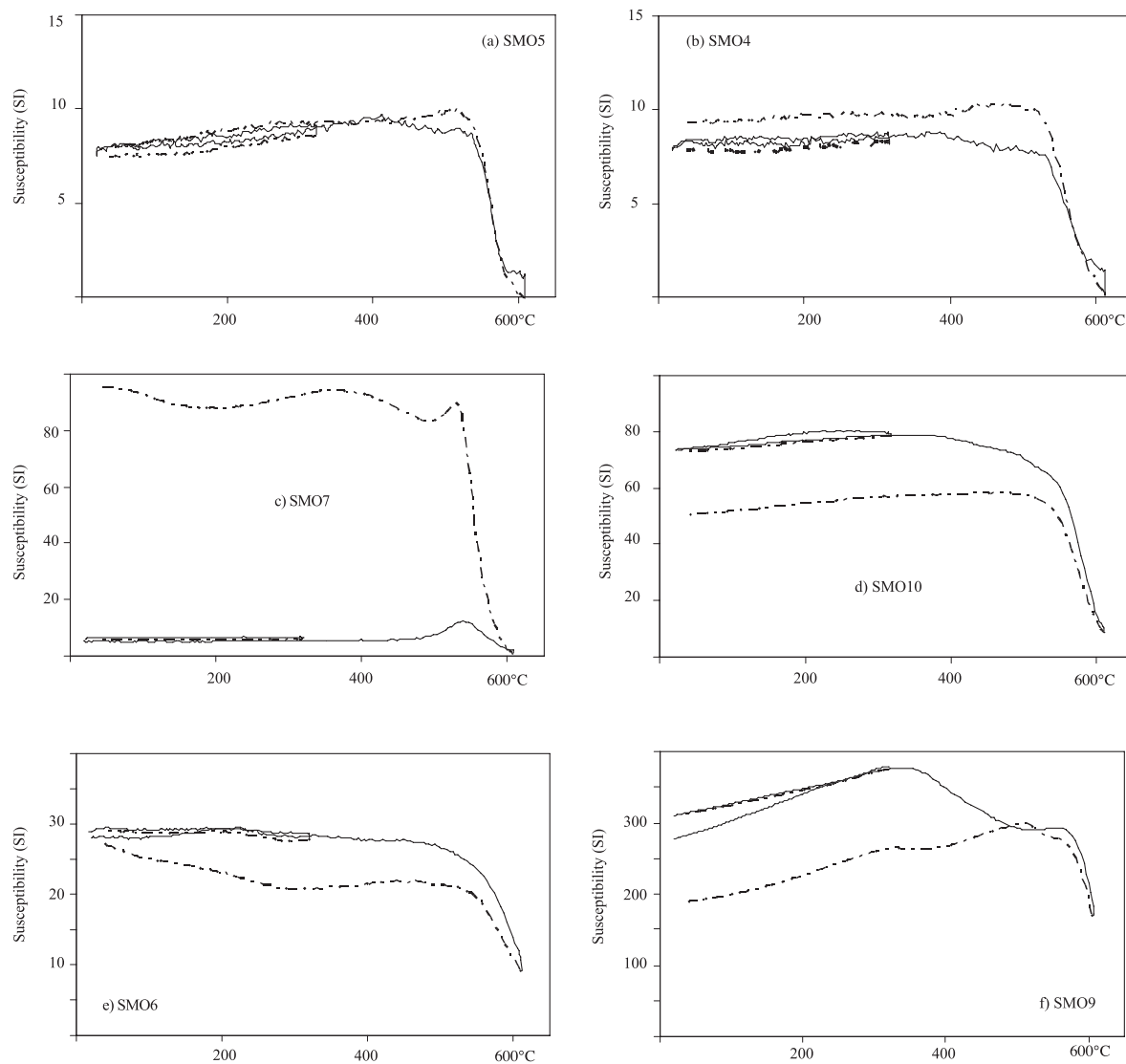


**Figure 12.** Variation of the low-field magnetic susceptibility versus temperature for SMO4, SMO5 and SMO7 ignimbrites, SMO6 and SMO9 basalts and SMO10 rhyolite. Two heating-cooling cycles have been performed, the first up to 320 °C and the second up to 600 °C.

are achieved only for thick flows emplaced at temperatures of at least  $\sim 660$  °C. In contrast, much lower density (between 1800 and 2000 kg m<sup>-3</sup>, diamonds in Fig. 15) characterizes samples for which no mean remanence per site could be estimated. These samples are likely to have been either emplaced at lower temperatures or mixed with air during transport resulting in possible oxidation that could explain the more complex nature of the magnetization carried by these rocks.

Mean directions were obtained from 7 of the 12 sampled sites; four with a normal polarity and three with a reverse magnetization. Considering the high temperature of emplacement estimated from the density of the samples from which a mean direction of magnetization was defined, this magnetization is likely to have been acquired during cooling of the rocks and is therefore representative of the time of emplacement of the SMO. This is further supported by the quality of the grouping at the cooling unit level and the positive reversal test.

If the stable magnetizations carried by our samples are indeed acquired as the volcanic rocks cooled shortly after eruption, the chronology of emplacement of the different units we sampled in the Oligocene can be further refined by comparing our data with the ge-

omagnetic polarity timescale GPTS (Ogg & Smith 2004, Fig. 16). Ignimbrite SMO4 was likely the first one to be emplaced during chron C12r (even though it is not possible to rule out the possibility of emplacement during chron C11r). Then basalt SMO9 was emplaced during chron C12n. The large uncertainty about the age of basalt SMO6 makes difficult to estimate the timing of emplacement, which could be either during chrons C12n, C11n or even C10n.2n. Ignimbrites SMO7 and SMO5 were then emplaced followed by the rhyolitic site SMO10 during chron C9r.

The SMO palaeopole is compared to the North America Synthetic Apparent Polar Path, calculated with a 10-Ma sliding window every 5 Ma (Fig. 17; Besse & Courtillot 2002). No overlap exists between the  $A_{95}$  associated with the Oligocene (28–31 Ma) SMO pole and any of the  $A_{95}$  associated with the 20–35 Ma intervals of the Master Path. Following the method of Demarest (1983), the net rotation values were estimated and a counter-clockwise vertical axis rotation of about  $10 \pm 4^\circ$  is indicated when compared with stable North America. As our only Miocene result is in perfect agreement with the Oligocene results, this rotation had to happen after emplacement of SMO2 ( $\sim 20$  Ma) and likely occurred during the third extensional episode in the Late Miocene (ca. 12–9 Ma).

**Table 3.** Palaeointensity results. ( $N$  and Interval) are, respectively, the number of steps and the temperature interval used in the calculation; ( $F$  and  $dF$ ) are the intensity and related standard deviation; ( $f$ ,  $g$ ,  $q$ ) are Coe (1967) quality factors for palaeointensity determinations. MAD is the maximum angular deviation around the least square estimation of the linear segment (Kirsink 1980) and  $\alpha$  is the angular difference between anchored and unanchored solutions.  $d(CK)$  (Leonhardt *et al.* 2004) and Drat (Selkin & Tauxe 2000) both give a relative measurement of the deviation between pTRM checks and the related pTRM value, normalized to the TRM in the first case and to the length of the selected segment in the second case.

Site	Sample	$N$	Interval	Class	$F$	$dF$	Slope	Linear fit criteria				Direction criteria		Alteration criteria	
								$SD$ (slope)	$f$	$g$	$q$	MAD	$\alpha$	$d(CK)$	Drat
SMO6 5/10 BAS	22	7	200–500	B	42.1	3.4	−1.40	0.08	0.70	0.77	6.7	0.9	0.8	5.4	4.5
	24	10	200–560	C	44.7	4.0	−1.49	0.09	0.36	0.83	3.4	1.5	4.2	8.8	13.5
	25	5	200–350	B	45.5	0.5	−1.52	0.01	0.43	0.66	26.8	0.6	0.6	2.1	2.7
	28	5	250–450	A	46.1	2.1	−1.54	0.05	0.74	0.48	8.0	1.2	0.9	3.4	2.5
	30	7	200–500	A	47.6	2.5	−1.59	0.05	0.62	0.80	9.3	3.0	4.8	4.1	3.5
					<b>45.2</b>	<b>2.0</b>									
SMO9 3/4 BAS	16	11	200–580	B	35.5	1.4	−1.18	0.04	0.68	0.84	14.4	1.1	0.7	6.3	5.9
	17	8	200–520	A	29.1	2.0	−0.97	0.07	0.43	0.81	5.1	1.5	0.9	4.6	7.7
	18	11	200–580	A	21	0.4	−0.70	0.02	0.60	0.87	25.3	1.0	0.3	3.0	4.1
					<b>28.5</b>	<b>7.3</b>									
SMO10 5/6 RHY	68	3	400–540	B	4.7	0.5	−0.16	0.10	0.56	0.72	3.8	7.9	11.4	2.2	1.3
	69	10	350–640	A	5.7	0.5	−0.19	0.09	0.92	0.87	9.4	5.6	5.7	3.3	3.5
	70	6	350–540	A	6.6	0.4	−0.22	0.07	0.61	0.77	7.0	3.5	2.5	1.6	2.6
	72	4	450–540	B	8.5	0.4	−0.28	0.04	0.25	0.64	3.8	1.4	0.7	1.9	7.3
	74	14	20–640	B	12.2	1.2	−0.41	0.10	0.38	0.88	3.4	2.4	8.6	3.5	8.5
					<b>7.5</b>	<b>3.0</b>									
SMO5 3/7 IGN	31	13	20–600	B	71.4	5.5	−2.38	0.08	0.41	0.88	4.6	1.3	5.7	6.6	6.2
	33	13	200–640	A	64.4	3.4	−2.15	0.05	0.56	0.83	8.8	0.8	1.4	3.0	2.3
	35	7	500–640	B	84.5	4.9	−2.82	0.06	0.37	0.57	3.7	0.8	0.3	6.9	6.2
					<b>73.5</b>	<b>10.2</b>									
SMO7 IGN 2/13	1	14	20–640	A	32.6	3.2	−1.09	0.10	0.88	0.58	5.1	3.7	3.8	4.0	3.1
	13	8	450–640	B	6.9	0.9	−0.23	0.13	0.69	0.64	3.4	1.3	0.2	5.5	7.8
					<b>19.8</b>	<b>18.2</b>									
SMO4 4/6 IGN	38	13	20–640	B	87.8	8.6	−2.93	0.10	0.64	0.81	5.3	0.9	1.5	4.6	2.3
	40	11	300–640	A	112.3	3.6	−3.74	0.03	0.92	0.60	17.2	1.0	0.1	2.8	0.8
	41	13	200–640	A	88.2	3.1	−2.94	0.04	0.83	0.61	14.1	1.2	1.2	1.9	0.7
	44	10	350–640	A	87.2	5.4	−2.91	0.06	0.56	0.77	6.9	1.2	2.2	4.7	2.7
					<b>93.9</b>	<b>12.3</b>									

Twenty-two palaeointensity estimates, which would be commonly considered as having good technical quality, were obtained out of the 47 measured samples. If we are fairly confident that the magnetization carried by our rocks was acquired during cooling, the nature of that magnetization is not so obvious. The temperature of emplacement estimated from the density measurements is high enough to allow acquisition during cooling by thermoremanent process. However, the magnetic carriers (titanomaghemite and hematite), the alteration seen under the microscope and the palaeointensity results (no internal consistency) all tend to point to a more complex nature of the magnetization with thermochemical remanent mechanism if not chemical remanent magnetization, likely because of the alteration of the rocks during and after emplacement (hydrothermalism). Apart, maybe, from one of the basaltic results (site SMO6) that exhibits not only good technical quality, but also the lowest degree of oxidation and internal consistency, all other results are questionable. Therefore, the SMO ignimbrites did not prove to be a good material for palaeointensity analysis.

Finally, even though we acknowledge that automatic calculation is indeed very convenient, we will go against the current trend, which is to suppose that they give more objective results. Even with extremely careful experimental or analytic analysis of the best thresholds to use for the chosen parameters, natural rocks are far too diverse and complex to allow a generalization of the thresholds.

Nothing can replace a critical analysis of the palaeointensity data, using all the background given by the geology, petrology, rock magnetic analysis and palaeomagnetic behaviour. As soon as the studied rocks depart from the ideal behaviour (pure TRM carried by single domain grains), any automatic selection can be misleading.

## CONCLUSIONS

(1) Two new  $^{40}\text{Ar}/^{39}\text{Ar}$  age determinations are reported for the Sierra Madre Occidental ignimbrites from sites SMO2 and SMO7, respectively at  $20.4 \pm 0.2$  and  $29.2 \pm 0.5$  Ma. Site SMO2 is the youngest ignimbrite so far dated. A patch of the Nayar ignimbrite sequence has therefore to be added in the middle of the Atengo formation shown between Huejuquilla and Las Canoas on the Ferrari *et al.* (2002) geologic map.

(2) A new 28–31 Ma mean palaeomagnetic direction and pole ( $N = 6^\circ$ ;  $\text{Dec} = 334.6^\circ$ ;  $\text{Inc} = 45.1^\circ$ ;  $\text{kappa} = 118$ ;  $\alpha_{95} = 6.2^\circ$ ;  $\text{Lat} = 66.8^\circ\text{N}$ ;  $\text{Long} = 180.5^\circ\text{E}$ ;  $\text{Kappa} = 142$ ;  $A_{95} = 6.3^\circ$ ) were calculated for the Sierra Madre Occidental. Comparison with the North America Synthetic Apparent Polar Path indicates a net counter-clockwise vertical axis rotation of about  $10 \pm 4^\circ$  compared to stable North America. This rotation occurred during the last extensional episode in the Late Miocene (ca. 12–9 Ma).

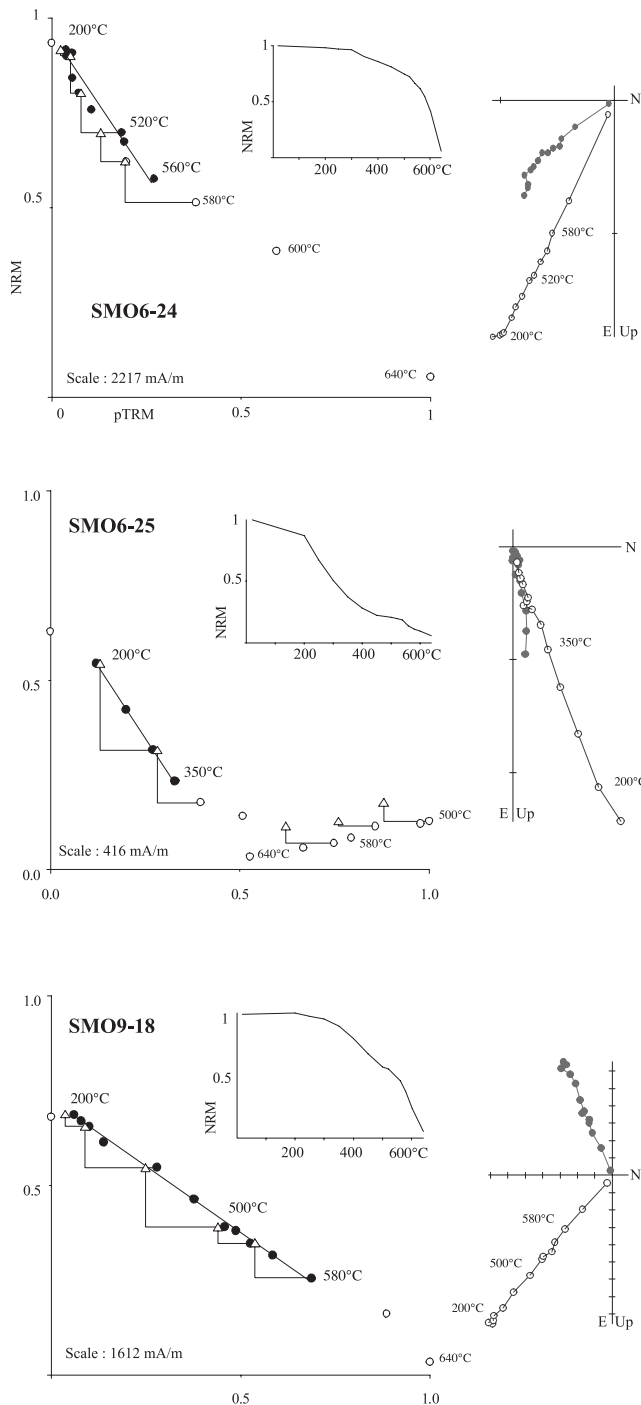


**Figure 13.** Representative palaeointensity diagrams (Arai plots, orthogonal diagrams in core coordinates and demagnetization curves) for the basaltic sites. Full (open) symbols are for data points used (not used) in the calculation of the linear fit.

(3) Density measurements, as a proxy for welding, proved to be extremely useful to estimate the emplacement temperature and the origin of the magnetizations carried by ignimbrites.

(4) Twenty palaeointensity estimates ranging from 4.7 to 112.3  $\mu\text{T}$  were obtained from the Sierra Madre Occidental samples. Except for the value ( $45.2 \pm 2.0 \mu\text{T}$ ,  $N = 5$ ) obtained from basaltic site SMO6, that is similar to the present-day field intensity and might be reliable, all other results are questionable and should not be used for global interpretation.

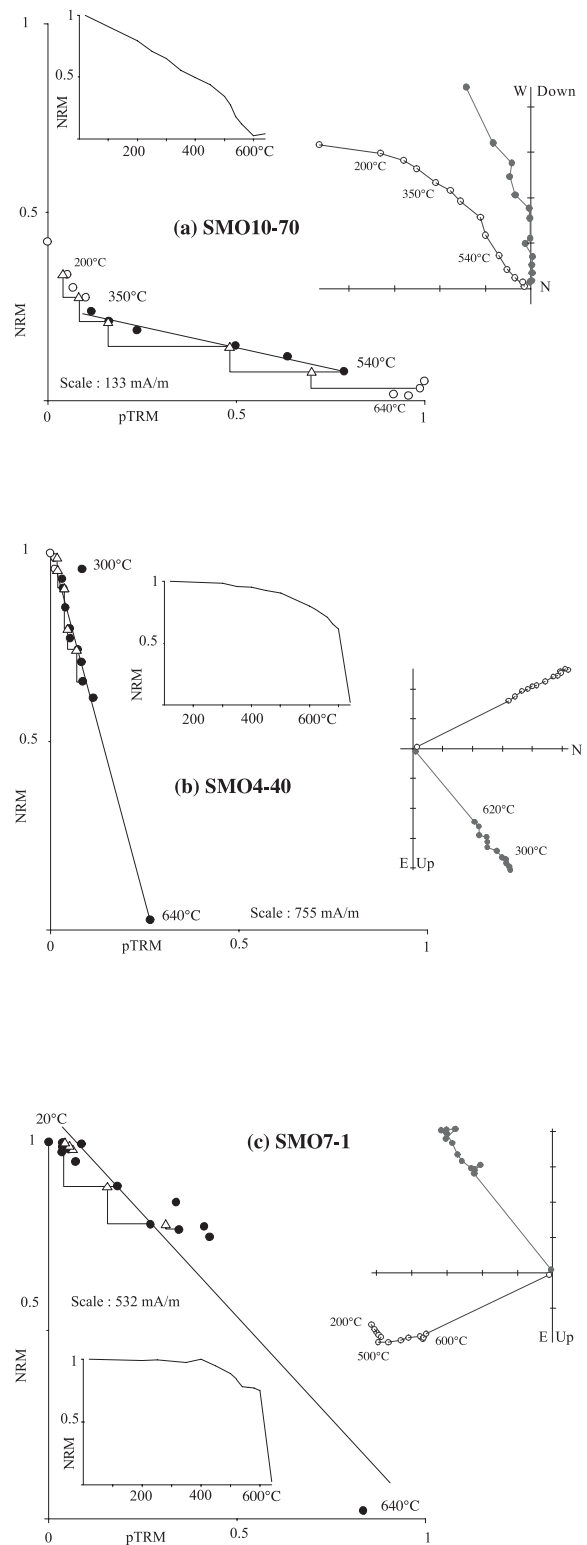


**Figure 14.** Representative palaeointensity diagrams (Arai plots, orthogonal diagrams in core coordinates and demagnetization curves) for the ignimbrites and the rhyolite. Full (open) symbols are for data points used (not used) in the calculation of the linear fit.

#### ACKNOWLEDGEMENTS

This research was funded through DGAPA-UNAM-IN110308 and CONACyT-105194 research projects, and INSU-CNRS PICS

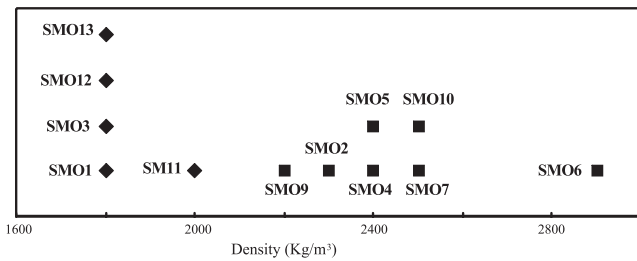


**Figure 15.** Density variation of the SMO ignimbrites. Squares (diamonds) are, respectively, for sites for which a mean direction of magnetization could (could not) be estimated.

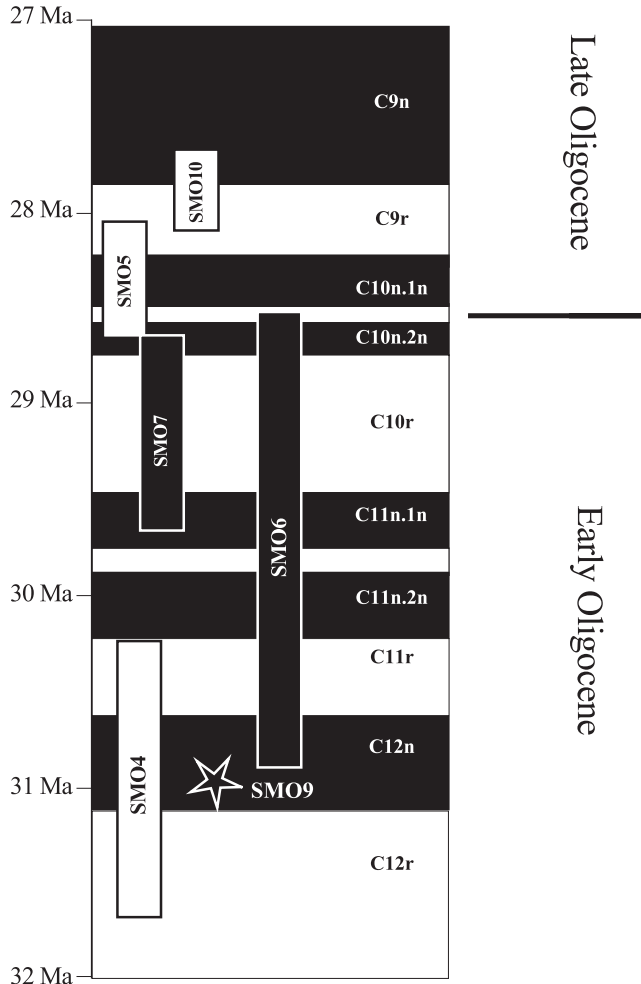


**Figure 16.** Correlation of the SMO palaeomagnetic polarities with the Geomagnetic Polarity Time Scale (Ogg & Smith 2004).

project 5319. We are grateful for laboratory support and thin-polished section microscope microphotographs to M. Rivas-Sanchez and C. Linares. Assistance in different aspects of the <sup>40</sup>Ar-<sup>39</sup>Ar experiments of M. García, A. S. Rosas-Montoya, G. Rendón-Márquez, V. Pérez-Arroyo and L. C. Gradilla-Martínez is also acknowledged. We are very grateful to G. Paterson and an anonymous reviewer for valuable comments that significantly improve the quality of the manuscript. The excellent editorial work of E. Petrovsky is finally acknowledged.

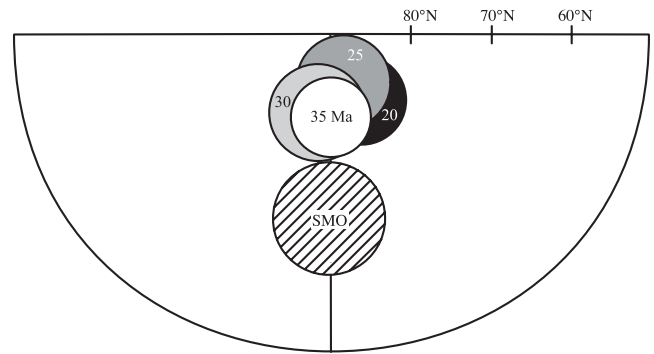


**Figure 17.** Comparison between the mean SMO Virtual Geomagnetic Pole and the 35–20 Ma section of the Master Polar Wander Path for Mexico (Besse & Courtillot 2002). All data are presented with their  $A_{95}$  circles of confidence.

**REFERENCES**

Alva-Valdivia, L.M., Rivas-Sanchez, M.L. & Perrin, M., submitted, Microscopy and rock magnetism of volcanic rocks through the southern part of Sierra Madre Occidental, Mexico, *Geofis. Int.*, in press.

Besse, J. & Courtillot, V., 2002. Apparent and true polar wander and the geometry of the geomagnetic field over the last 200 Myr, *J. geophys. Res.*, **107**(B11), 2300–2332.

Biggin, A.J., Perrin, M. & Dekkers, M.J., 2007. A reliable absolute paleointensity determination obtained from a non-ideal recorder, *Earth planet. Sci. Lett.*, **257**, 545–563.

Bryan, S.E., Riley, T.R., Jerram, D.A., Leat, P.T. & Sepsens, C.J., 2002. Silicic volcanism: an undervalued component of the large igneous provinces and volcanic rifted margins, in *Magmatic Rifted Margins*, pp. 97–118, eds Menzies, M.A., Klemperer, S.L., Ebinger, C.J. & Baker, J., Geol. Soc. Am. Spec. Paper 362.

Coe, R.S., 1967. Paleointensities of the Earth’s magnetic field determined from Tertiary and Quaternary rocks, *J. geophys. Res.*, **72**, 3247–3262.

Day, R., Fuller, M. & Schmidt, V.A., 1977. Hysteresis properties of titanomagnetites: grain size and compositional dependence, *Phys. Earth planet. Inter.*, **13**, 260–267.

Demarest, H.H., 1983. Error analysis for the determination of tectonic rotation from paleomagnetic data, *J. geophys. Res.*, **88**, 4321–4328.

Draeger, U., Prevot, M., Poidras, T. & Riisager, J., 2006. Single-domain chemical, thermochemical and thermal remanences in a basaltic rock, *Geophys. J. Int.*, **166**, 12–32.

Fabian, K., 2009. Thermochemical remanence acquisition in single-domain particle ensembles: A case for possible overestimation of the geomagnetic paleointensity, *Geoch. Geophys. Geosyst.*, **10**, Q06Z03, doi:10.1029/2009GC002420.

Ferrari, L. & Rosas-Elguera, J., 2000. Late Miocene to Quaternary Extension at the Northern Boundary of the Jalisco Block, western Mexico: The Tepic-Zacoalco rift revised, in *Cenozoic Tectonics and Volcanism of Mexico*, pp. 41–64, eds Delgado-Granados, H., Aguirre-Díaz, G.J. & Stock, J.M., Geol. Soc. Am. Spec. Paper 334.

Ferrari, L., López-Martínez, M. & Rosas-Elguera, J., 2002. Ignimbrite flare-up and deformation in the southern Sierra Madre Occidental, western Mexico—implications for the late subduction history of the Farallon Plate, *Tectonics*, **21**, doi:10.1029/2001TC001302.

Ferrari, L., Valencia-Moreno, M. & Bryan, S., 2007. Magmatism and tectonics of the Sierra Madre Occidental and its relation with the evolution of the western margin of North America, *Geol. Soc. Am. Sp. Paper*, **442**, 1–39.

Gee, J.S., Yu, Y. & Bowles, J., 2010. Paleointensity estimates from ignimbrites: an evaluation of the Bishop Tuff, *Geoch. Geophys. Geosyst.*, **11**, Q03010, doi:10.1029/2009GC002834.

Henry, C.D. & Aranda-Gómez, J.J., 2000. Plate interactions control middle-late Miocene proto-Gulf and Basin and Range extension in the southern Basin and Range, *Tectonophysics*, **318**, 1–26.

- Hoffman, K.A., Singer, B.S., Camps, P., Hansen, L.N., Johnson, K.A., Clipperton, S. & Carvallo, C., 2008. Stability of mantle control over dynamo flux since the mid-Cenozoic Phys, *Earth Planet. Int.*, **169**, 20–27.
- Kirsivink, J.L., 1980. The least-squares line and plane and the analysis of paleomagnetic data, *Geophys. J. R. astr. Soc.*, **62**, 699–718.
- Leonhardt, R., Heunemann, C. & Krása, D., 2004. Analyzing absolute paleointensity determinations: acceptance criteria and the software ThellierTool 4.0, *Geoch. Geophys. Geosyst.*, **5**, Q12016, doi:10.1029/2004GC000807.
- Masliwec, A., 1984. Applicability of the  $^{40}\text{Ar}/^{39}\text{Ar}$  method to the dating of ore bodies, *PhD thesis*, University of Toronto, Canada.
- McDowell, F.W. & Clabaugh, S.E., 1979. Ignimbrites of the Sierra Madre Occidental and their relation to the tectonic history of western Mexico, in *Ash-Flow Tuffs*, pp. 113–124, eds Chapin, C.E. & Elston, W.E., Geol. Soc. Am. Spec. Paper 180.
- McFadden, P.L. & McElhinny, M.W., 1990. Classification of the reversal test in palaeomagnetism, *Geophys. J. Int.*, **103**, 725–729.
- Nieto-Samaniego, A.F., Ferrari, L., Alaniz-Alvarez, S.A., Labarthe-Hernández, G. & Rosas-Elguera, J., 1999. Variation of Cenozoic extension and volcanism across the southern Sierra Madre Occidental volcanic province, Mexico, *Bull. geol. Soc. Am.*, **111**, 347–363.
- Ogg, J.G. & Smith, A.G., 2004. The geomagnetic polarity time scale, in *A Geologic Time Scale 2004*, Vol. 24, pp. 63–86, eds Gradstein, F.M., Ogg, J.G. & Smith, A.G., Cambridge University Press, Cambridge.
- Prévot, M., Mankinen, E.A., Coe, R.S. & Grommé, C.S., 1985. The Steens Mountain (Oregon) geomagnetic polarity transition, 2, field intensity variations and discussion of reversal models, *J. geophys. Res.*, **90**, 10 417–10 448.
- Riehle, J.R., Miller, T.F. & Bailey, R.A., 1995. Cooling, degassing and compaction of rhyolitic ash flow tuffs: a computational model, *Bull. Volcanol.*, **57**, 319–336.
- Roberts, A., Cui, Y. & Verosub, K., 1995. Wasp-waisted hysteresis loops: mineral magnetic characteristics and discrimination of components in mixed magnetic systems, *J. geophys. Res.*, **100**, 17 909–17 924.
- Selkin, P.A. & Tauxe, L., 2000. Long-term variations in palaeointensity, *Phil. Trans. R. Soc., Lond.*, **358**, 1065–1088.
- Steiger, R.H. & Jäger, E., 1977. Subcommittee on Geochronology: convention on the use of decay constants in Geo and Cosmochronology, *Earth planet. Sci. Lett.*, **36**, 359–362.
- Tauxe, L., 2010. *Essentials of paleomagnetism*, University of California Press, Berkeley.
- Tauxe, L., Mullender, T. & Pick, T., 1996. Potbellies, wasp-waists, and superparamagnetism in magnetic hysteresis, *J. geophys. Res.*, **101**, 571–583.
- Thellier, E. & Thellier, O., 1959. Sur l'intensité du champ magnétique terrestre dans le passé historique et géologique, *Ann. Geophys.*, **15**, 285–376.
- Wasilewski, P.J., 1973. Magnetic hysteresis in natural materials, *Earth planet. Sci. Lett.*, **20**, 67–72.
- York, D., Evensen, N.M., López-Martínez, M. & De Basabe-Delgado, J., 2004. Unified equations for the slope, intercept, and standard errors of the best straight line, *Am. J. Phys.*, **73**, 367–375.
- Zhang, C., Paterson, G.A. & Liu, Q., 2012. A new mechanism for the magnetic enhancement of hematite during heating: the role of clay minerals, *Stud. Geophys. Geod.*, **56**(3), 845–860.